Journal of Materials Chemistry B

ROYAL SOCIETY OF CHEMISTRY

PAPER

View Article Online
View Journal | View Issue

Cite this: *J. Mater. Chem. B*, 2021, **9**, 4941

Shape anisotropic magnetic thrombolytic actuators: synthesis and systematic behavior study†

Maxim A. Zakharzhevskii, ‡[a] Elizaveta I. Anastasova,‡[a] Daniil V. Kladko, ‡[a] Artur Y. Prilepskii, ‡[a] Maria N. Gorshkova,[a] Denis A. Vinnik,[b] Sergey V. Taskaev[bc] and Vladimir V. Vinogradov *[a]

Received 9th April 2021,
Accepted 3rd June 2021

DOI: 10.1039/d1tb00783a

rsc.li/materials-b

Thrombosis-related diseases are undoubtedly the deadliest disorders. During the last decades, numerous attempts were made to reduce the overall death rate and severe complications caused by treatment delays. Significant progress has been made in the development of nanostructured thrombolytics, especially magnetically controlled. The emergence of thrombolytic magnetic actuators, which can deliver tPA to the occlusion zone and perform mechanical disruption of the fibrin network under the application of a rotating magnetic field (RMF), can be considered for the next generation of thrombolytic drugs. Thus, we propose a systematic study of magnetic-field mediated mechanically-assisted thrombolysis (MFMMAT) for the first time. Four types of magnetic particles with different morphology and dimensionality were utilized to assess their impact on model clot lysis under different RMF parameters. Chain-like 1D and sea urchins-like 3D structures were found to be the most effective, increasing thrombolysis efficacy to nearly 200%. The drastic difference was also observed during the dissolution of 3 days old blood clots. Pure plasminogen activator had almost no effect on clot structure during 30 minutes of treatment while applying MFMMAT led to the significant decrease of clot area, thus uncovering the possibility of deep venous thrombosis therapy.

1. Introduction

Every year strokes and other cardiovascular diseases lead the World Health Organization's mortality ratings.[1] Some of the socially-important diseases are also accompanied by thrombosis complications.[2] Nowadays, surgery remains the primary approach for thrombus removal despite all its drawbacks and contraindications. The use of thrombolytic enzymes is quite limited due to the main side effect of this therapy – systemic fibrinolysis and consequent hemorrhagic stroke. Also, 13% of the strokes are hemorrhagic by nature, and the use of thrombolytics for hemorrhagic cases can be fatal.[3] However, 87% of the cases potentially can be treated with thrombolytics. On the other hand, the high rate of inhibition of thrombolytic enzymes and their low diffusion into the fibrin clot drastically decrease the effectiveness of treatment. The overcoming of the issues mentioned above could be found in lowering the dose of thrombolytic agents and localization of the lysis effect.

Over the past ten years, there have been several attempts to replace classical fibrinolytics with synthetic or natural proteins. For example, desmoteplase from bats is currently undergoing clinical trials.[4] However, modern science is not limited to the search for new enzymatic agents and is continuously exploring alternative directions such as drug delivery techniques and other ways of dissolving blood clots.

Drug delivery systems are of considerable importance due to the possibility of increasing the thrombolytic concentration at the occlusion site, thus reducing hemorrhagic side effects. Advances in micro- and nanoscience give birth to some micro- and nanoformulated thrombolytics developments, for instance, in the form of liposomes,[5] hydrogels,[6] polymer capsules,[7–9] and even virus-based[10] or erythrocyte-derived particles.[11]

Alternatively, inorganic particles can be used instead of organic capsules. There are several advantages of nanoparticles, such as stability, low cost, and the ability to control particles *via* external stimuli, for instance, magnetic field. The FDA-approved magnetite (Fe_3O_4) holds a special place among all targeted drug delivery materials due to its biodegradability, biosafety, and high magnetic moment.[12] Over the past few decades, many systems for

[a] *International Institute "Solution Chemistry of Advanced Materials and Technology", ITMO University, St. Petersburg 197101, Russia. E-mail: vinogradov@scamt-itmo.ru*
[b] *National Research South Ural State University, Chelyabinsk 454080, Russia*
[c] *Chelyabinsk State University, Chelyabinsk 454001, Russia*

† Electronic supplementary information (ESI) available. See DOI: 10.1039/d1tb00783a

‡ These authors contributed equally.

magnetic delivery of thrombolytic agents containing magnetite nanoparticles have been developed.[13–16] Another essential property of the drug delivery systems is the protection of a drug from inhibition in blood flow.[17] A magnetic field is also of interest since it can be utilized for a broad range of stimuli due to magnetic field energy conversion to thermal or mechanical influences by magnetic actuators. Under the effect of an alternating (AMF) or rotating (RMF) magnetic field, the magnetic actuators start to move due to the magnetic moment of particles to follow the external magnetic field's direction.

However, there are few works dedicated to the evaluation of RMF-assisted thrombolysis. Recently, it was shown that Ni and Fe_3O_4 anisotropic microparticles in combination with an RMF make it possible to enhance the thrombolytic activity of t-PA.[18,19] The increase in thrombolysis rate (TR) was explained by the possibility of a controlled release of a thrombolytic drug and the acceleration of mass transfer due to nanoparticle carrier rotation. It was suggested that the impact of mechanically induced clot rupture could not be the major. However, in 2017 Tansci *et al.* proved that magnetic microwheels following the corkscrew trajectories could mechanically interact with the thrombus, penetrate the fibrin mesh, and weaken its structure.[20] Even though the impact of mechanical actuation was proved for the first time, many questions arose about the effect, shape, size, composition of particles, the nature, and age of the fibrin clot. Still, the mechanical damage of thrombus by magnetic particles under the magnetic field's action remains unclear and debatable. Thus, it becomes necessary to conduct a systematic study that determines mechanical actuation in thrombolytic systems.

Herein, we provide a systematic study of magnetic field-mediated mechanically-assisted thrombolysis (MFMMAT) focusing on: (1) comparison of the efficacy of 0D, 1D, 2D, and 3D magnetic actuators prepared by newly developed methods and based on FDA-approved magnetite; (2) explanation of a detailed mechanism for particle-mediated clot lysis; (3) demonstration of the MFMMAT ability to dissolve even thrombolytic-resistant 3 days old blood clots, thus uncovering the possibility for deep venous thrombosis (DVT) therapy; (4) showing that MFMMAT is independent on thrombolytic type using two different thrombolytic enzymes, single-chain urokinase plasminogen activator (scuPA) and tissue plasminogen activator (alteplase) in flow conditions.

2. Results and discussion

2.1. Synthesis and characterization of particles

To study the effect of particle shape-anisotropy during MFMMAT, we developed and synthesized systems based on magnetite of various dimensions. We chose magnetite because it is FDA-approved and is used clinically as an MRI contrast agent in products such as Endorem™, Feridex®, and Resovist®.[21] It is known that changes in the morphology of Fe_3O_4 particles can lead to a variation in their physical and chemical properties and are strongly dependent on the synthetic protocol chosen for their production.[22] As a reference sample, we used well-characterized magnetite nanoparticles, designated as 0D.[23] 0D nanomaterials are mostly spherical or quasi-spherical nanoparticles with a diameter of about 10 nm.[24,25] General requirements for anisotropy structures are high saturation magnetization and pronounced shape anisotropy for effective magnetic control *via* RMF. 1D particles were synthesized in the form of long chains, 2D particles as plates, and 3D as spiky spheres. Another debatable issue is the choice of synthesis methods for all four types of structures. Bearing in mind the biomedical application of our particles, a distinctive feature of the synthesis should be simplicity, reproducibility, and low-toxic precursors usage.

The schematic representation of the synthesis methods used in this work and SEM microphotographs of all synthesized samples are presented in Fig. 1, while the schemes of particle formation are shown in Fig. S1 (ESI†). A detailed mechanism of particle formation is provided in ESI.† A simple and effective method of co-precipitation of iron(II) and (III) chlorides allows us to synthesize the magnetite nanoparticles up to 20 nm in diameter at room temperature (Fig. 1A).[26] Their plane projection belongs to zero-dimensional structures. According to XRD spectra (Fig. 1E), the crystal lattice corresponds to magnetite (compared to JCPDS file No. 19-0629). The sample shows peaks, indicating the ultra-fine small crystallite size of the particles. Scherrer equation analysis indicates that the magnetite crystallites' average size is 10 nm, consistent with SEM microphotographs (Fig. 1A).

The 1D particles were synthesized in the shape of long chains by a modified self-assembly pathway (Fig. 1B).[27,28] Significant advantages of the 1D particles are their extraordinary length, flexibility, and structure that can easily bend into various shapes. The procedure involves synthesising 1D particles by reducing iron(III) chloride by a strong reducing agent such as sodium borohydride.[29] The synthesized particles served as seeds which subsequently line up in long chains (Fig. S1, ESI†). As can be seen from SEM micrographs (Fig. 1B), the length and width of Fe_3O_4 particles were in the range of 1–11 μm and 0.1–0.5 μm, respectively. The length-to-width ratio of 1D particles allows us to consider them as 1D structures, with a width close to that of 0D particles. The X-ray diffraction analysis of the material (Fig. 1E) revealed that magnetite is the main component of the sample (70%), with other phases, iron 8% (α-Fe) and iron boride 22% (FeB) (compared with JCPDS files No. 19-0629, 96-900-6600, 96-400-3013, respectively). The presence of organic coating, as expected, led to a decrease in the signal-to-noise ratio, which, however, did not prevent the phase from being uniquely identified.

For the fabrication of magnetite 2D plates, we, for the first time, demonstrated a single-step facile approach using a soft chemical route. The idea behind the synthesis of two-dimensional structures (plates) was based on the Ostwald ripening process with hydrothermal treatment and additional stabilization of aqueous magnetite particles with citric acid. Citric acid is one type of low molecular weight chelate compound that acts as a complexing reagent controlling nanomaterials' shape and growth[30] and preventing particles' agglomeration.[31] A part of carboxyl groups substituted magnetite particles surface hydroxyl groups and formed a monomolecular adsorption layer, which reduces the

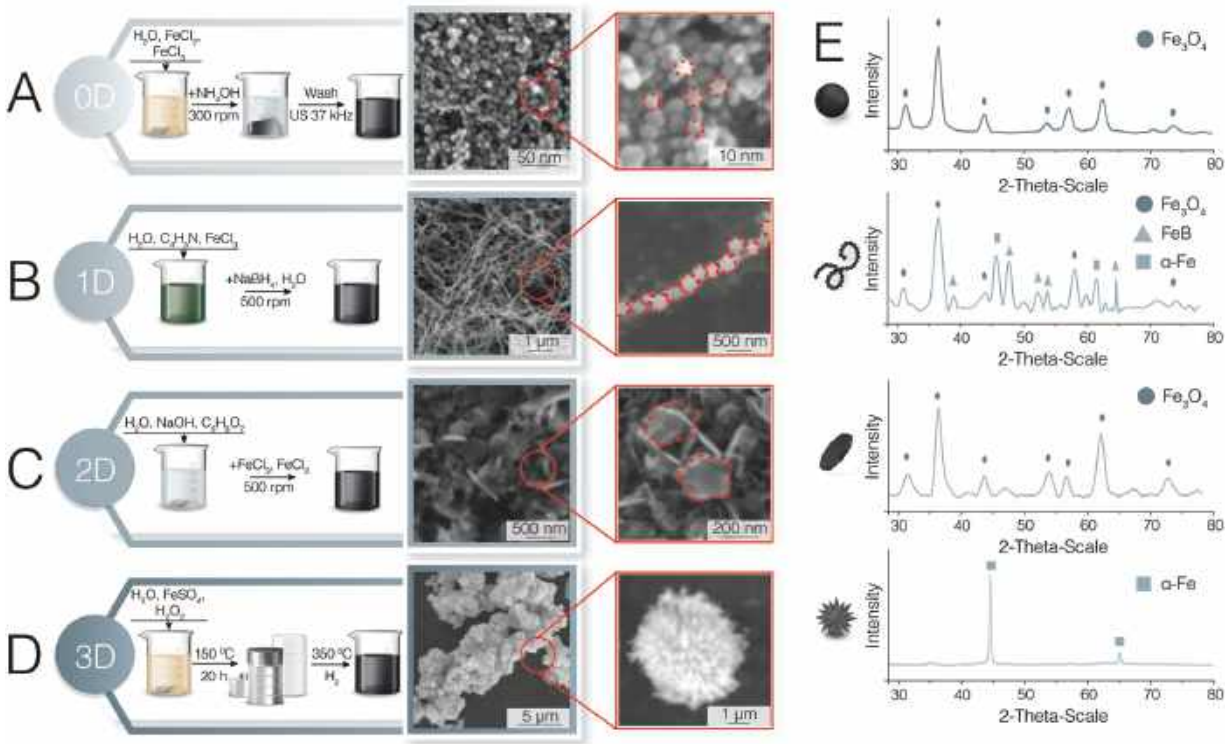

Fig. 1 The synthesis scheme of shape-anisotropic structures and SEM micrographs of the resulting particles. (A) 0D nanoparticles. According to SEM micrographs, co-precipitation of iron chlorides(II) and (III) produces 0D nanoparticles of ~15 nm in diameter. (B) 1D chains. Self-assembly of magnetite nanoparticles in the presence of pyrrole leads to the formation of long (up to 11 μm) chains with a thickness of 100–500 nm. (C) 2D plates. Using citric acid as a coating agent allows us to synthesize thin (15 nm according to SEM) plates with a width up to 250 nm. (D) 3D sea urchins-like particles. A two-stage synthesis method, including hydrothermal synthesis of goethite and its reduction in a stream of dry hydrogen, leads to the formation of 3D particles up to 5 μm in size. (E) X-Ray diffraction patterns of the prepared anisotropic structures. The main phase in 0D, 1D, and 2D particles is magnetite, while 3D particles are 90% iron and 10% magnetite. Peaks of iron and iron boride are also presented in a 1D pattern.

reaction rate and inhibits grain growth.[32] The stoichiometric co-precipitation of iron(II) and iron(III) chlorides (Fe^{2+}/Fe^{3+} molar ratio = 2) was carried out in the water in the presence of citric acid ligand (5 mmol). The subsequent addition of a base, ammonium hydroxide, leads to the formation of a black precipitate. According to SEM images (Fig. 1C), the resulting plate diameter lies in the range of 200–300 nm, while the average thickness is 15 nm. The XRD analysis (Fig. 1E) of the 2D particles showed that magnetite is the main phase with a crystallite size of 200 nm. 2D particles were the only one investigated particle types with a negative surface charge (Table 1). The negative charge was associated with the adsorption of COO^- groups, left from citric acid, on the surface of the particles.

We synthesized particles with a complex 3D structure frequently called «sea urchins» to obtain the complete picture of anisotropy influence. The development of the one-pot synthesis of such complex particles seems to be very challenging. Therefore, it was decided to divide the synthesis into two stages. In the first step, goethite (α-FeOOH) particles of the required shape and diameter up to 5 μm were obtained (Fig. S2, ESI†). It should be noted that the goethite crystallizes in the form of needles (length of needles ~100 nm according to SEM micrographs) on the surface of the particle, which determines the morphology of the sea urchin-like particles. In the second step, the goethite was reduced in the stream of dry hydrogen at 350 °C to obtain the required phase composition. As a result, spiky polyphase particles with a size of up to 5 μm were obtained (Fig. 1D). The crystal lattice of obtained material according to XRD spectra (Fig. 1E) corresponds to magnetite (phase fraction 10%, JCPDS file No. 19-0629) and α-Fe (phase fraction 90%, JCPDS file No. 6-696).

Table 1 Main physico-chemical parameters of used particles

Particle type	Average size	ζ-Potential, mV	Crystallite size, nm	Main phase, %	The saturation magnetization (M_s), emu g^{-1}	Remanent magnetization (M_r), emu g^{-1}	Coercivity (H_c), Oe
0D	5–10 nm	36 ± 2	10 ± 2.1	100% Fe_3O_4	70	9	169
1D	1–11 μm length, 0.1–0.5 μm width	30 ± 3	20 ± 4.8	70% Fe_3O_4	115	11	178
2D	200–300 nm in diameter, 15 nm thickness	−14 ± 2	200 ± 40	100% Fe_3O_4	50	2	27
3D	Up to 5 μm in diameter	12 ± 2	35 ± 7	90% α-Fe	155	31	550

Magnetic properties of particles play a crucial role considering MFMMAT. The room temperature magnetic hysteresis loops are shown in Fig. 2A. The nonlinear hysteresis loops with small nonzero remanent magnetization (M_r) and coercivity (H_c) show well pronounced superparamagnetic properties for 0D, 1D, and 2D actuators. The hysteresis loop with higher M_r and H_c for 3D actuator shows the ferromagnetic properties with the multidomain composition. The saturation magnetization (M_s), remanent magnetization (M_r), and coercivity (H_c) for magnetic actuators are presented in Table 1. Obtained results imply that the relatively strong magnetic response to the external magnetic field is achieved. A decrease in M_s for 0D and 2D objects is observed compared to bulk magnetite (92 emu g^{-1}),[33] which can be attributed to the surface contributions.[34] The high M_s for the 1D object (115 emu g^{-1}) might correspond to iron and iron boride in the sample, which is confirmed by XRD data (see Fig. 1E). The highest M_s for the 3D object (155 emu g^{-1}) is in good agreement with XRD data (Fig. 1E), and the reference value for M_s for bulk iron 217.6 emu g^{-1}.[35] The inset of Fig. 2A displays the zoom region between −600 and 600 Oe to showing the hysteresis loops more clearly.

Zero-field cooled (ZFC) and field cooled (FC) temperature dependencies (Fig. 2B) revealed the main feature of superparamagnetism, such as broad maximum at T_{max}, representing average blocking temperature (T_B). The blocking temperatures for 0D, 1D, and 2D particles are 249 K, 102 K, and 217 K, respectively. ZFC and FC curves exhibit broad maxima, resulting from interparticle interaction and broad particle size distribution, correlated with SEM images and XRD data. With known blocking temperature and mean particle volume, it is possible to extract the effective anisotropic constant (K_{eff}) from ZFC/FC measurements and estimate the anisotropic energy of particles.[36] The K_{eff} for 0D, 1D, and 2D particles are 0.4 kJ m^{-3}, 0.02 kJ m^{-3}, and 0.0012 kJ m^{-3}, respectively, which interplay between the type of magnetic anisotropy and size for different magnetic actuators.[37] The 3D particle exhibits the absence of the blocking temperature, which confirm the ferromagnetic nature of this particle type.

2.2. Cytotoxicity assessment

Preliminary evaluation of the obtained structures' cytotoxic properties is critical since the new synthesis methods were used. Cytotoxicity was assessed through the standard MTT metabolic assay on HCT116 cells (human colon carcinoma) for 72 hours. The results are presented in Fig. 3. We did not observe any significant cytotoxicity signs for 0D, 2D, and 3D particles in all studied concentrations (except ~20% decrease for 3D particles after 72 hours). The obtained results are in good agreement with available data taking into account that the particles are composed of biocompatible magnetite according to XRD (Fig. 1E). A rather different result was observed for 1D particles, which were significantly cytotoxic at high concentrations. At 400 and 200 μg mL^{-1}, the decrease in metabolic activity was about 70%. A 100 μg mL^{-1} concentration leads to a 40% decrease in metabolic activity, while already at a concentration of 50 μg mL^{-1}, no cytotoxicity was observed. Observed cytotoxicity cannot be attributed to FeB or polypyrrole in composition since both are biocompatible.[38,39] Possibly, cytotoxicity is caused by α-Fe found on XRD spectra.

Simultaneously, 3D particles, which are mostly α-Fe in composition, do not cause such cytotoxicity. However, toxicity can be caused by other than composition reasons.[40] A further study should be carried to investigate the detailed mechanism underlying the cytotoxicity of 1D particles, which is not in the course of this work. For subsequent experiments, concentrations equivalent to human dose ~5 mg L^{-1} will be used.

2.3. General principles of thrombolysis mediation by magnetic particles

It is known that the external RMF forces paramagnetic particles to chain up and rotate as a single structure.[41] In our work, we focused on dimensional-anisotropic 0–3D magnetic particles. Such particles

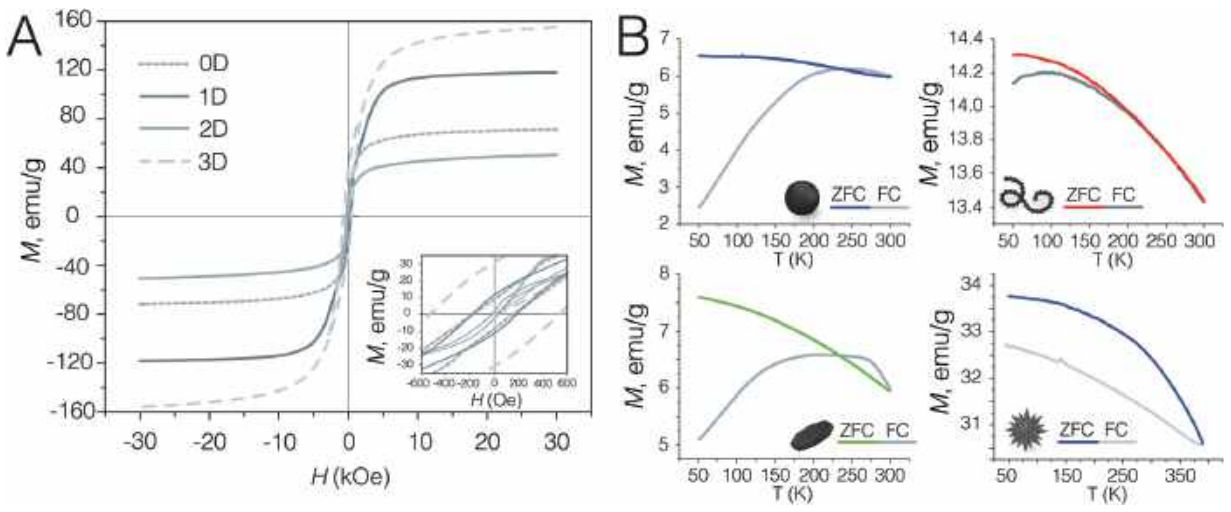

Fig. 2 (A) The room temperature magnetic hysteresis loops of the particles with different shapes. On inset: enlarged fragment of hysteresis loops showing −600 to 600 Oe region. (B) The temperature-dependent zero-field cooled (ZFC) and field cooled (FC) curves under an applied field of 200 Oe and temperature between 50 K and 400 K for the magnetic actuators of different shapes. The colored part of the curves corresponds to ZFC, while the grey-scale part corresponds to FC.

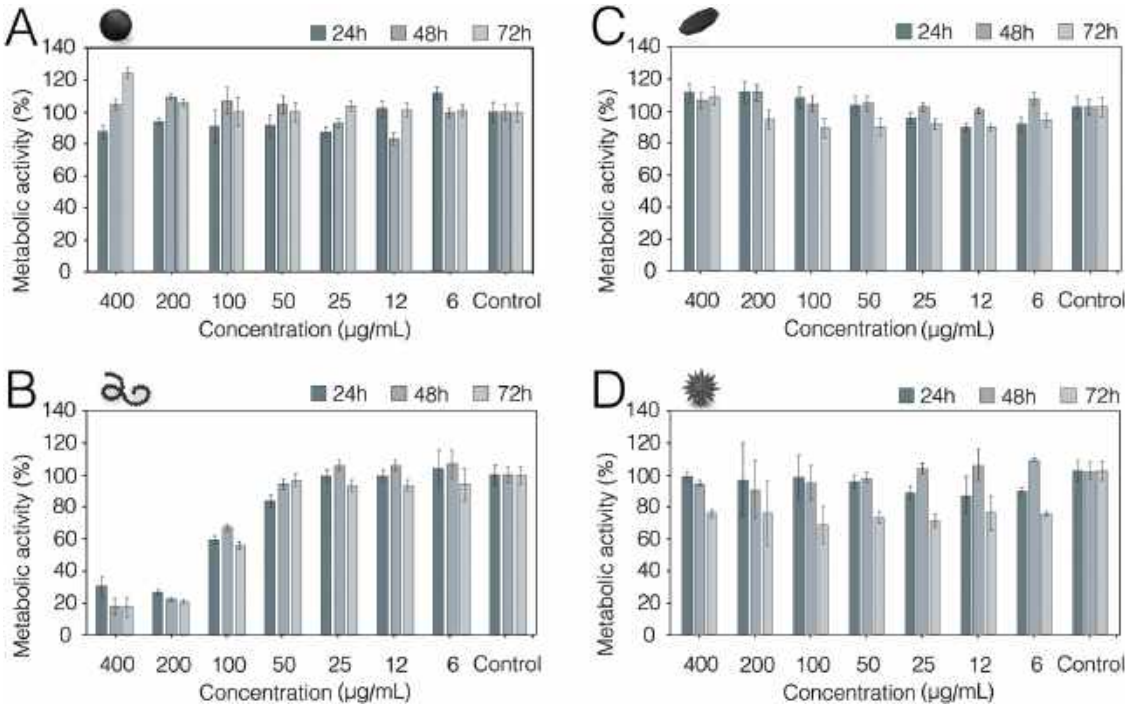

Fig. 3 Metabolic activity of HCT116 cells measured by MTT assay after incubation with different particles. (A) 0D particles. No obvious signs of cytotoxicity were observed. ~20% increase of activity after 72 hours at high concentration can be attributed to particle adsorption on wells bottom and their interference with optical density. (B) 1D particles were found to be cytotoxic at high concentrations, LC50 ≈ 100 μg mL^{-1}, LOEC = 50 μg mL^{-1}, NOEC = 25 μg mL^{-1}. (C) 2D particles. Similar to 0D particles, no cytotoxicity was observed. After 72 hours, a small decrease of about 10–15% was detected, which is not essential to cell viability. (D) 3D particles. Only a ~20% decrease in the activity was observed after 72 hours of incubation, which was concentration-independent.

with different morphology can behave uniquely under RMF. However, due to the difference in physico-chemical characteristics, their impact on the clot structure may be completely contrasting.

Current research data did not allow researchers to fully understand the mechanism of thrombolysis enhancement by ferrimagnetic particles through exposure to an AMF.[42] We suggested two possible mechanisms. Firstly, we expect that the rotating magnetic particles and their aggregates will affect the fluid flow, increasing the diffusion and mass transfer in the clot's proximity. Secondly, particles could mechanically affect clots and increase fibrin permeability for thrombolytic agents. Moreover, we advocate that these effects are strictly interconnected and cannot be studied separately. Thus, we attempted to bring forward the importance of the synergistic effect from particles in thrombosis treatment for the first time.

To understand what stimuli are needed to enhance thrombolysis, the limitations of thrombolytic therapy must be considered. One of the main limitations is the inhibition of plasmin by alpha 2-antiplasmin.[43] Plasmin should form in abundance within the clot, where it is protected from the inhibitors. Thus, the main difficulty here is the transport of thrombolytic to the internal structures of the thrombus. Fibrin fibrils form a mesh that is impenetrable by plasmin or other fibrin-nonspecific enzymes. Therefore, the first limitation of thrombolytic therapy has a mechanical background.

In our work, we build up a model experiment considering a case close to large vessel occlusion (LVO).[44] The blood flow in the affected vessel is nearly absent, and additional factors begin to influence the rate of thrombolysis. The interaction between thrombolytic molecules in the blood and a thrombus represents a heterogeneous system. One of the critical limiting factors for reaction kinetics in a heterogeneous system is the frequency of collisions between molecules. The reaction course can be increased by mixing the system.[45] Given the almost complete absence of blood flow in the vessel, mixing can only be executed at the micro-level. Therefore, the second limitation of thrombolytic therapy has hydrodynamic nature.

For mixing purposes, magnetic particles of various shapes are widely used.[46] At the micro-level, their behavior is described by Mason numbers (M_n).[47] These numbers characterize the ratio of magnetic force to viscosity force and operate at the individual particle level.[48] Moreover, the application of RMF with a magnitude lower than coercivity field induces the formation of micro- or macro-scale vortices.[49] It is noteworthy that $M_n > 1$ required for the transition of single particle rotation to micro-vortex assembly.[47] This phenomenon could alter the hydrodynamic flow around the clot and therefore changes the TR. However, the mixing efficiency of such a micro-vortex is limited by the external magnetic field's frequency.[50] Therefore, we have been expecting the threshold frequency, after which the efficacy of RMF-assisted thrombolysis, enforced by mixing, will increase at a slower rate.[51]

To summarize, we need to overcome the clot's rigidity and bring mixing to the thrombus area. Both of these can be realized by rotating magnetic particles. According to our assumption,

shape-anisotropic particles can closely interact with clot fibrils and disrupt the fibrin mesh, allowing thrombolytics to penetrate deeper into the clot. Simultaneously, particles' rotation and their micro-vortex assembly will create fluid flows causing a thrombolytic mass transfer. To study the different effects and assess the contribution of each of them separately, we used the different particle shapes, RMF frequency, concentrations of particles, and thrombolytic concentration.

2.4. Dependence of thrombolysis rate from the shape and frequency

We initially started our investigation from the evaluation of particles anisotropy impact. The schemes of our RMF experimental setup and particle behavior under the external magnetic field are shown in Fig. 4. The experiment is described in detail in the Methods section. Briefly, particles with different morphologies were poured on the clot along with a scuPA solution. No preliminary conjugation between scuPA and particles was used. The concentration of the particles and scuPA remains the same (20 mg mL^{-1} and 0.8 mg mL^{-1}, respectively). The relatively high particle concentration ensures vortex formation in the clot area.[41] For convenient data presentation, we decided to evaluate the lysis effectiveness within a 12 minutes interval after the addition of thrombolytic composition. Such an interval was chosen because, in some preliminary experiments, the clot completely dissolves within this time. The effectiveness of lysis was assessed by measuring the clot area. Firstly, the rate of fibrin clot lysis by pure scuPA was measured. The TR with particles was calculated and normalized by the pure scuPA TR, set as 100%. The results are presented in Fig. 5.

The first step was to analyze the effectiveness of 0D particles and set them as a reference point. In the absence of RMF, the 0D particles have no significant effect on thrombolytic activity. The 0D particles are shape-isotropic and possess relatively strong dipole–dipole interaction, which prevents the rotation of chains assembly at the high particle concentration.[52] Consequently, the application of RMF in the whole frequency range does not affect the efficiency of thrombolysis (the difference between frequencies is less than the experimental error). For 1D particles, we observed an inhibition of the TR in the absence of RMF by 34 ± 8%. To a first approximation, this can be explained by the sorption of a thrombolytic agent not only on the positively charged magnetite but also on polypyrrole strands. While it seems undesirable, we consider this inhibition fortunate because outside of the RMF area, scuPA would not exhibit severe side effects. However, the application of the RMF significantly increases the system's thrombolytic activity in a frequency-dependent manner, by 36 ± 8% at 12 Hz and up to 68–70 ± 8% at 50–100 Hz. The application of the RMF with a frequency of 200 Hz increases the TR by 76 ± 10% compared to free scuPA.

The 2D particles have not shown considerable inhibition of TR upon the addition of particles without RMF (even a 26 ± 8% increase was observed). We associate this effect with a much lower ζ-potential of particles and their negative charge (Table 1), which have prevented the adsorption of scuPA. Also, the effect of RMF was lower in the 12–100 Hz range compared to 1D particles (13–33%) and had no difference compared to the RMF-off condition. The maximum TR for 2D particles was 43 ± 6% at

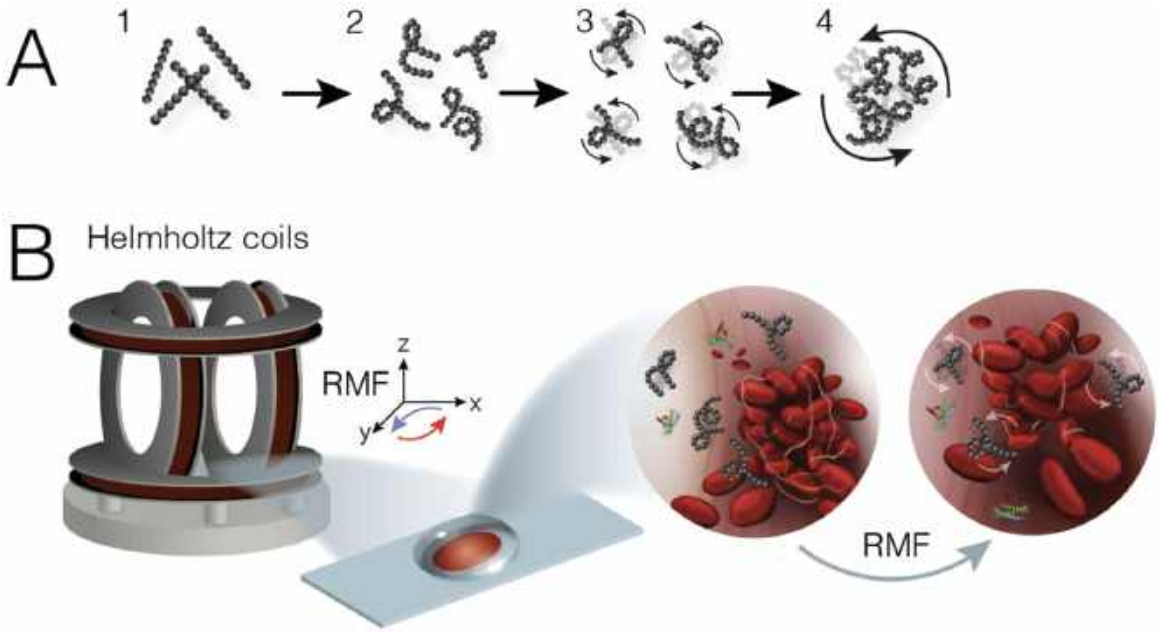

Fig. 4 (A) The scheme of particle behavior under RMF. (1) Particles are dispersed in media. (2) After numerous switches of RMF orientation, chains become twisted and (3) start to rotate. (4) Inner flows of closely positioned rotating chains are zeroed and summarized outer flow is formed, leading to vortex formation. (B) The scheme of the MFMMAT setup. The model clot is placed on a cover glass inside the experimental chamber. The chamber is located in the center of three axially-positioned Helmholtz coils. RMF is generated in the horizontal plane (*i.e.*, *XY* plane). scuPA solution along with tested particles is poured on top of the clot. Upon application of RMF, the abovementioned process of vortex formation starts, and the clot began to dissolve.

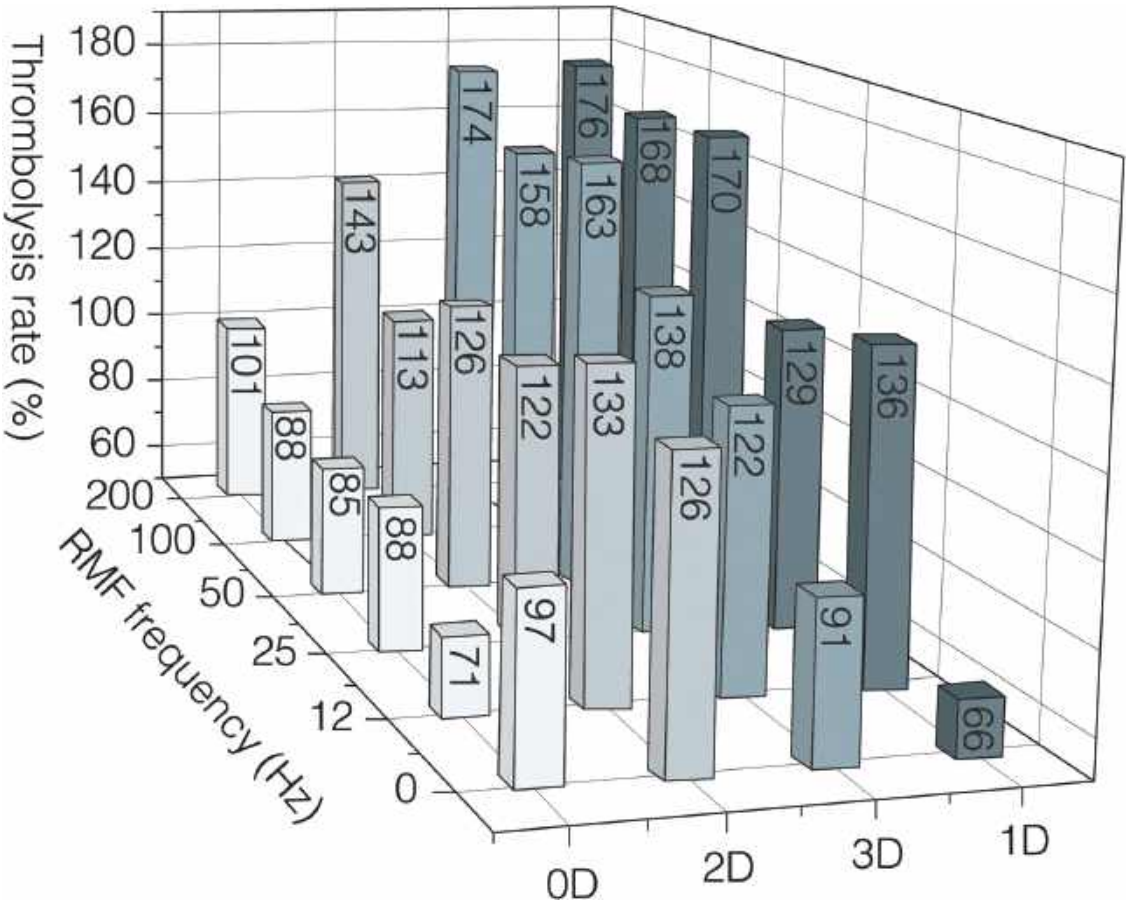

Fig. 5 Dependencies of thrombolysis rate (TR) from the RMF frequency and shape of particles. TR for pure scuPA set as 100%. 0D particles inhibited TR at almost all frequencies possible due to the electrostatic binding of scuPA to particles. The same reason leads to a TR decrease for 1D and 3D without RMF. 2D particles with different surface charges did not display such inhibition behavior. Upon application of RMF, no TR increase was observed for 0D structures due to their shape isotropy. All other systems demonstrate a varying degree of TR increase, basically in a frequency-dependent manner with 1D and 3D particles performing almost identically.

200 Hz. For 3D particles, we observed pretty similar behavior as for 1D particles. In the absence of the RMF, the TR remained the same compared to scuPA, while the application of RMF increased the TR by 22–58% in the 12–100 Hz range. The most effective enhancement of thrombolysis was at 200 Hz, with the TR increased by 174 ± 16%.

Thus, the 1D and 3D particles provide the highest TR increase among the presented systems. This allows us to assert that the shape anisotropy of particles plays a crucial role in MFMMAT. An important parameter is the magnetization of particles, which is much higher for 1D and 3D structures (Table 1). However, the TR dependence from ζ-potential and real-time lysis monitoring reveals some exciting connections between shape, charge, and frequency parameters, which will be further discussed. For further experiments, we chose 1D particles for several reasons. Despite the apparent cytotoxicity at higher concentrations, a predicted final concentration for intravenous use would be not higher than 5 μg mL^{-1}. Also, 1D particles are much easier to synthesize, and the final yield is significantly higher. The magnetic properties of 1D particles are much more promising than those of 3D. The difference in M_s between 1D and 3D particles is significant (115 *vs.* 155 emu g^{-1}), but the 3D particles exhibit the higher value of M_r and H_c. Such parameters could complicate their use in MFMMAT therapy due to strong dipole interaction between particles without a magnetic field. Our observations have shown that 3D particles tend to aggregate in the physiological medium. Still, the 1D particle has a much stronger response to the magnetic field than 0D and 2D particles and has a superparamagnetic nature, unlike 3D particles. Additionally, the chain-like structure of 1D particles proves to be beneficial, as will be discussed further.

2.5. The features of mixing at low frequencies

One of the most intriguing questions connected with thrombolysis's mechanical actuation is the balance between effects of mixing and mechanical rupture of fibrin mesh. It is needed to determine the actual cause of mixing to understand the impact of mixing. When an external rotating magnetic field was applied, the neighboring magnetic 1D and 3D particles produced two-dimensional vortex-like structures. The formation mechanism of such vortices was recently described in detail.[50] Briefly, the process of vortex formation is connected with the superposition

of microfluidic flow forces around rotating particles (Fig. 4A). Upon application of the RMF, chains start to turn to align with the external magnetic field, which results in twisting the chain and creating a micro vortex around it. We assume that the chain-like structure of our 1D particles is quite beneficial at the stage of twisting. Contrary to the chain formed by dipole–dipole interaction, the as-synthesized 1D chain is more durable; thus, the resulting vortex is also more stable. More importantly, we observed that the formation of vortex structures is even more complicated. When multiple micro vortices are located close to each other, the inner flows are zeroed. However, external flows sum up and result in a single vortex, with observable millimeter-scale size (Video S1, ESI†).

To evaluate the contribution of these vortices into the TR increase, we precisely studied their rotation characteristics. It was previously shown that the mixing ability of such vortices strongly depends on their shape, which, in return, depends on the frequency of the external magnetic field.[41] We captured videos *via* a high-speed camera to assess the correlation between the external frequency of RMF and the rotation frequency of particles and vortices. The results are presented in Fig. 6A. The frequency of separate particles is closely correlated with the RMF frequency (Fig. 6B). Due to the media's low viscosity, only slight differences were observed (*e.g.*, at 200 Hz, particles rotate at 193 Hz). We further found that vortices are forming only at boundary frequencies. No vortices were detected in the range of 1–10 Hz due to the very slow rotation of magnetic particles. More vortices appear with the RMF frequency increasing. According to the available data, the maximum mixing ability corresponds to circle-shaped vortices, which occur at a frequency below 30 Hz.[41] Already after 50 Hz, vortices frequency decreases. In our case of 1D particles, stable vortices were observed until 100 Hz. It is important to note that vortices rotation was quite different from particle rotation in terms of the distribution of rotation speeds. Some of the vortices rotate very slowly (*i.e.*, 2 Hz at 50 Hz external frequency) while others rotate much faster (*i.e.*, 9 Hz at 50 Hz external frequency). The broad distribution of vortices rotation speed caused a significant standard deviation in Fig. 6B.

Nevertheless, the increase/decrease trend of the rotation speed is observable. Vortices and particles rotation speed dependencies from external frequency explain the results presented in Fig. 6B. According to our investigation, a significant increase in TR (by 60–70%) was observed when relatively low-frequency RMF ($<$100 Hz) was applied to a clot. This increase mainly corresponds to the rise of mixing speed by vortices. The vital question to ask is, what happens at external frequency $>$100 Hz?

2.6. The features of mixing at high frequencies

At the external frequency of 100 Hz, stable vortices still exist. However, at 200 Hz, almost no vortices were observed, and the existing vortices rotated at a very slow speed. The explanation of this phenomenon lies in the behavior of a single particle. Due to the media's viscosity, particles cannot completely follow the magnetic field orientation changes, so they shake instead of rotating. Still, some of the elongated aggregates, with low surface section, can rotate and form vortices. Simultaneously, formed vortices were spontaneously contracting and flocculating (Fig. 6A, 200 Hz). Upon flocculation, rotation frequency increases drastically, risen to near 200 Hz (as of a single particle). Thus, the behavior of the system at 200 Hz changes dramatically.

Even though almost no vortices exist at 200 Hz, floccules can also provide mixing (Fig. 6C). We assessed the effective radius of mixing as a ratio of floccules radius ($r1$) to the mixed area radius ($r2$) (Fig. 6D). It turns out that bigger floccules ($r1 \sim 90$ μm) provide more inferior mixing efficacy (low $r2/r1$ ratio, mixing radius $\sim$350 μm, $r2/r1 \approx 4$), while smaller floccules ($r1 \sim 40$ μm)

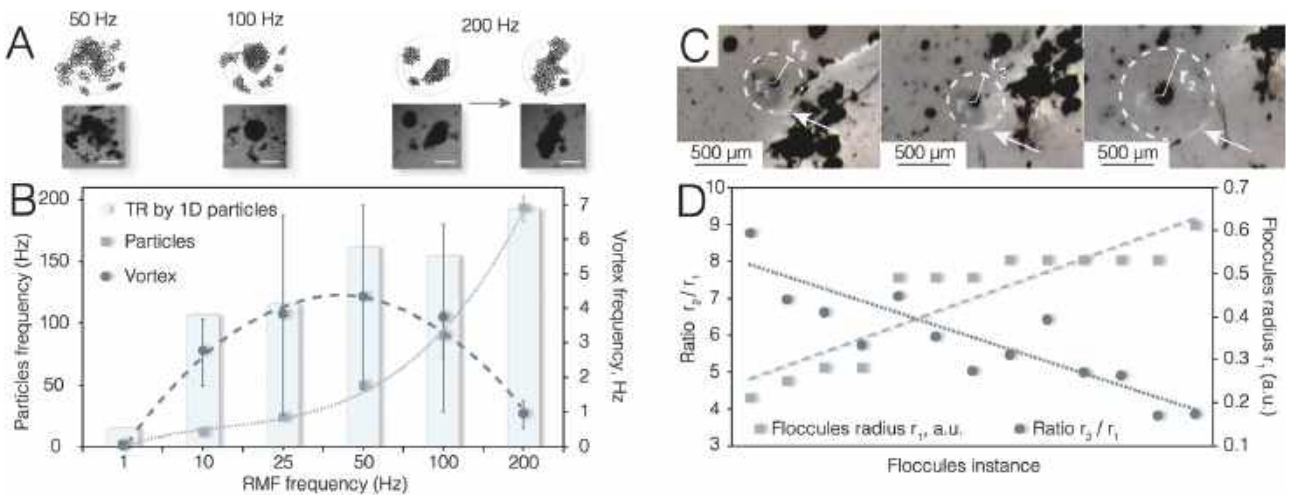

Fig. 6 (A) Schematic representation and actual images of rotating vortexes at different RMF frequencies. The more stable and fast-moving vortexes were detected at 50 Hz. A further increase to 100 Hz leads to a denser vortex core. At 200 Hz, vortices collapsing into floccules which continues to rotate. The scale bar is 25 μm. (B) Dependence of the 1D particles and vortices frequency from the RMF frequency. Histogram showing TR by 1D particles and scaled for better representation. (C) A visual appearance of mixing floccule. White dashed circle marking the mixed area border, while an arrow pointing at the vortex track (visible as a white arc). The floccule radius is marked as $r1$, and the mixing area radius is marked as $r2$. (D) Correlation between floccules radius $r1$ and $r2/r1$ ratio, showing a linear increase in mixing efficacy when the $r1$ is decreasing.

mix the media twice better (mixing radius ~330 μm, $r2/r1 \approx 8$). Therefore, the mixed area was 15 times bigger than the size of the floccules. Notably, the mixed area by single floccule was significantly (at least three times) smaller than that of a vortex in all cases. Nevertheless, the mixing effect still occurs at high frequencies and contributes to the overall TR increase.

The effect of mixing is seen in Video S2 (ESI†): vortices pass along the clot border, and visible reduction of the clot area is observed. However, until this moment, we did not focus on the subject of mixing, *i.e.*, "what" is mixed by particles. There are two possible ways of how mixing can increase TR. Actual images and proposed schemes for this effect are presented in Fig. 7A and B. Firstly, more scuPA molecules are transferred to the clot to interact with plasminogen on the clot surface. ζ-Potential plays an essential role in this process. scuPA molecules become electrostatically entrapped inside floccules, and upon passing the clot, some of them can interact with fibrin mesh. Secondly, the lysis products, predominantly fibrin fragments (D-dimers), are washed away from the clot, exposing the inner intact fibrin fibrils for thrombolytics. However, from Fig. 6B, it is seen that when the external frequency exceeds 50 Hz, TR still increases but at a much lower rate. This increase cannot be attributed to a mixing effect alone because vortices speed is decreasing. Thus, we assume that disruptive mechanical effects came into play at higher frequencies.

2.7. The interconnection between mixing and mechanical impact at high frequency

The estimation of mechanical impact can be executed in two ways. The first is to change scuPA or particle concentration, and the second is to investigate the interaction of particles with clot precisely.

Scrupulous investigation of the lysis patterns showed that the lysis occurs much faster in the areas where the clot border is disturbed by rotating particles. In Video S2 (ESI†), such an area is encircled. Disturbance of the clot border is an essential step in the initial stage of thrombolysis. In Fig. 7C and D, the intact edge of a fibrin clot is shown.

As can be seen, fibrin fibrils are stacked along the clot border, forming a wall and protecting the inner structure. Because fibrils thickness directly depends on thrombin concentration, which is present in media, surface fibrils are thinner but denser.[53,54] In this sense, physical disruption of surface fibrils should be beneficial for further lysis. To prove our suggestions, we measured the clot TR in terms of clot area reduction. The clot border, abundantly covered with particles, presumably will be disturbed by their movements. Indeed, as shown in Fig. 7E, lysis occurs much faster in disturbed border areas (clot in Fig. 7E is the same as in Fig. 7C). The lysis front propagates at 5 times faster speed in the region covered and disturbed by particles.

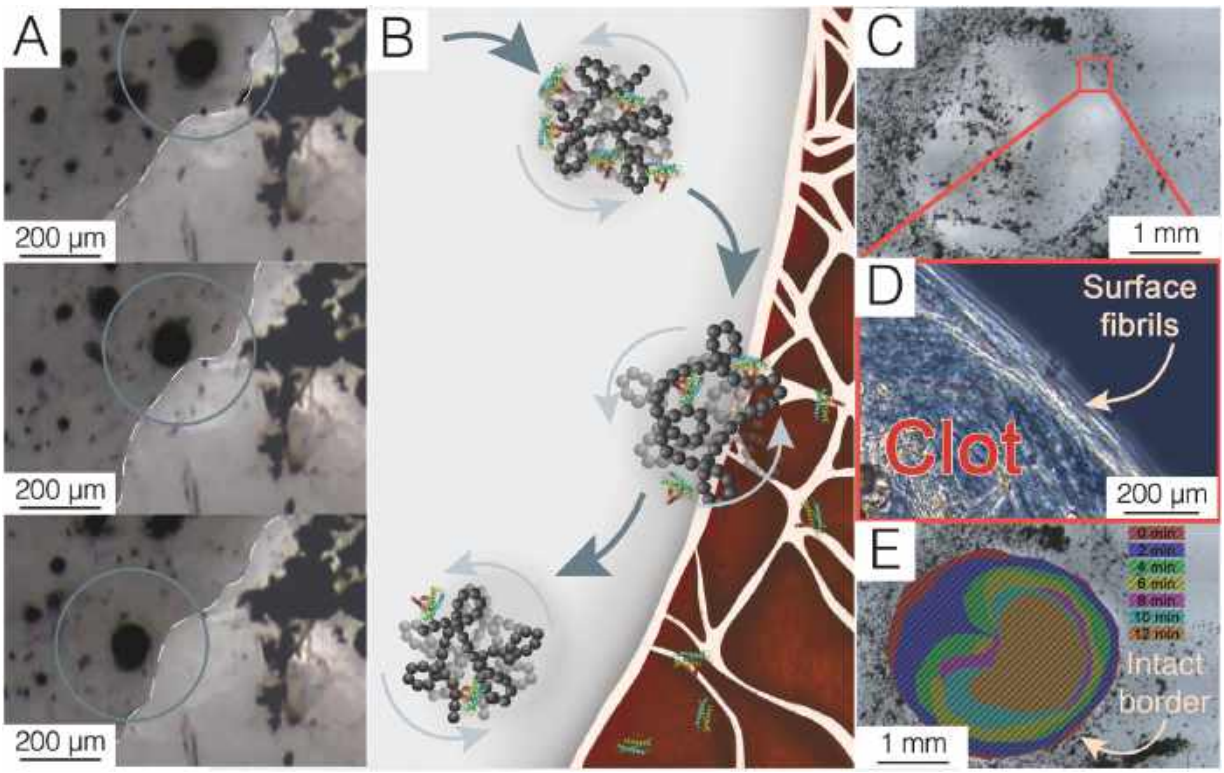

Fig. 7 (A) Actual images of the mixing process. Rotating floccules are passing along the clot border (marked by dashed lines). The mixed area is marked with a grey circle. (B) The corresponding scheme of the mixing process. Electrostatically entrapped scuPA came to the clot's proximity, where some molecules interact with fibrin and cause lysis. The vortex is passing further, taking out lysis products from the clot. (C) Macro image of the clot, showing the intact border area marked with a red square. (D) The enlarged image in phase-contrast mode, showing the fibrin clot and fibrils orientation on the clot's border. Surface fibrils are stacked along the clot border and are denser than in the rest of the clot. (E) The progress of the clot lysis over time, showing the difference between lysis speed near areas disturbed by particle movements and intact borders.

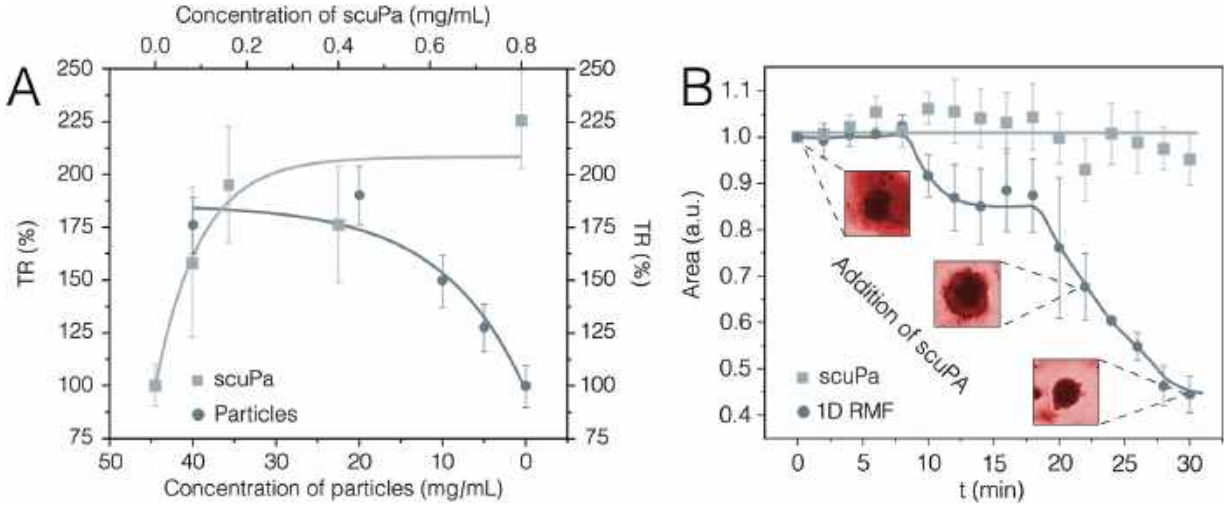

Fig. 8 (A) TR by 1D particles with different particles and scuPA concentrations. TR was found to have a horizontal plateau after 0.4 mg mL^{-1} of scuPA, showing no further increase. Rising particles concentration above 20 mg mL^{-1} can lead to a slight increase in TR; however, the experimental error also increases. (B) Lysis of aged blood clot in terms of clot area reduction. No lysis was observed when the blood clot was exposed to a pure scuPA solution. When particles accompanied scuPA, lysis of 60% clot area was observed within 30 minutes.

To further confirm our suggestion on the importance of mechanical effect, we evaluated TR in experiments with one fixed parameter. In the first experiment, we fixed scuPA concentration and varied particle concentration from 0 to 40 mg mL^{-1} (the typical concentration for other experiments was 20 mg mL^{-1}). We observed that the experimental error increases significantly with increasing particle concentration (Fig. 8A). Simultaneously, only a slight concentration dependence was discovered for concentrations above 20 mg mL^{-1}, accompanied by a rapid increase of the error. Mainly for this reason for all experiments, we used a concentration of 20 mg mL^{-1} as a compromise between repeatability and effectiveness.

We fixed particle concentration and varied scuPA concentration from 0.08 to 0.8 mg mL^{-1} in the second experiment. We observed that even at a tenfold lower concentration, particles could increase TR by 25% (Fig. 8A). However, as we stated earlier, mechanical and mixing (*i.e.*, enzymatic) effects are closely interconnected. The most intriguing question left to be answered is whether particles can damage fibrin filaments or are they not strong enough?

2.8. Torque forces for different shapes in RMF

From slow-motion videos, it was observed that both floccules and particles vigorously shake when they are entrapped within the clot. Nevertheless, some authors stated that magnetic particles could not damage fibrin fibrils directly.[55] However, the feature of magneto-mechanical action of particles on clot fibrin mesh must be considered. From a magnetism point, it is well known that on a magnetic particle with the magnetic moment μ in a magnetic field with flux density B acts the torque:

$$M = \mu \times B = VM_sB \quad (1)$$

where V – the volume of a particle, M_s – saturation magnetization of a particle, and B – magnetic flux density.

As were described earlier, the magnetic torque applied to the biopolymer surface is counterbalanced by the restoring forces that originate from the elasticity of the surface.[56] From this point of view, the ratio of magnetic torque to elastic torque of clot could be a criterion to evaluate the possibility of increasing fibrin mesh size. This ratio (k) could be expressed as followed:

$$k = \frac{M}{\tau_e} = \frac{VM_SB}{S^2G}L \quad (2)$$

where S – the area of network mesh, G – elastic modulus, L – length of the deformed element. By choosing L equal to the particle diameter, G (3 Pa) as elastic modulus of test clot,[57] and size of network mesh equal to 3 μm,[57] we estimate the ratio of the torque k. The $k \ll 1$ describes the case when the magneto-mechanical action of particles has no chance to change the mechanical properties of fibrin mesh. $k < 1$ demonstrates the possibility of increasing mesh size under the magneto-mechanical force's action with a high loading rate. Here it should be noted that clot elastic modulus can be changed during thrombolysis. This can change the situation from $k < 1$ to $k \geq 1$. $k \geq 1$ is a requirement for the magnetic torque force to induce a significant change in the fibrin network. The ratio of torques for 0D, 1D, 2D, and 3D particles are 9.6×10^{-6}, 0.3, 0.001, and 2.8, respectively. From the calculation, we can conclude that magneto-mechanical torque from 3D particles could deform the fibrin network mesh of the thrombus. However, the previous study provides information about a significant decrease of clot elastic modulus during thrombolysis, enhancing the magnetic torque action on fibrin network mesh upon RMF-mediated lysis.[58] The fibrin mesh size plays an important role in TR: the diffusion of scuPA into the thrombus depends on the clot's pore size.[59] From this perspective, the magneto-mechanical action could change the fibrin-fibrin distance and increase thrombolytic diffusion into the clot.

The abovementioned quasi-static estimation does not show the correlation between the magnetic field frequency and TR.

As discussed earlier by Le-Deygen *et al.*, the high loading rate is proportional to the frequency and force action of particles in the presence of the alternating magnetic field.[60] Following this suggestion, the mechanical rupture force from magnetic actuators under RMF could be significantly higher than under a static magnetic field. Therefore, the increase in TR is a consequence of the number of loading cycles of particles (which directly depends on the RMF frequency and time). This suggestion could be proven because 2D particles, which do not form vortices, still add a 40% increase in TR compared to scuPA alone at 200 Hz frequency. The 0D particles, as a magnetically isotropic object, possess neither mixing nor magneto-mechanical action. As expected, no influence on TR by 0D particles was observed. The movie S4 (ESI†) of 3D particles-mediated thrombolysis shows the significant movement of clot border under the action of RMF, and vortices at 200 Hz from 3D particle also were not observed.

2.9. Lysis of aged blood clot

The obtained results allowed us to suggest that the developed approach can be applied in the field of venous thrombosis. Application of RMF to whole limbs is more convenient than the localization of separate arteries; magnetic targeting of particles is also easier under slow blood flow in veins. Nowadays, the utilization of thrombolytics to treat deep vein thrombosis (DVT) is one of the most underrated thrombolytics applications. The severity of DVT is well known and causes about 100 000 deaths yearly only in the USA.[61] There are several significant differences between the treatment of acute arterial thrombosis and venous thrombosis. Firstly, vein clots, in most cases, form for a longer time and contain a whole spectrum of blood cells.[62] They are much more resistant to thrombolytics action and require continued treatment with a drug injection for several days.[63] Secondly, the treatment window for vein thrombolysis is much broader and not narrowed to 3–4.5 hours as for arterial thrombolysis.[64] It is almost always beneficial to have a vein clot dissolved, regardless of how long it exists.[65] However, due to fibrin crosslinking by factor XIIIa, old blood clots are invulnerable to dissolution.[66] Also, the side effects of prolonged systemic thrombolytic therapy are considered to be too undesirable for further clinical use.[67]

We attempted to lyse blood clots formed naturally from vein blood for three days. The results are presented in Fig. 8B. A drastic difference was observed between pure scuPA and actuated by 1D particles under RMF. During the experiment, we added scuPA to the clot three times (at 10 minutes interval). After the addition of the transparent enzyme solution, the clot's border becomes more visible, which results in a more accurate calculation of the clot area and "steps" on the clot area plot. Pure scuPA has almost no effect on clot structure. We observed only small fluctuations of the clot area caused by hemolysis of erythrocytes. The total shrinkage of the clot area after 30 minutes was no more than 5%. Contrary, we detected a considerable shrinking of the clot area by 60% under RMF. Using the blood clot, we also clearly observed the homogenization effect of the magnetic particle's vortices (video S3, ESI†). Moreover, particles stuck in a blood clot during lysis can be reactivated if their surrounding was dissolved. It is worth noting that since magnetic particles partially penetrate the thrombus, the front of lysis propagates along the clot's edges and inside it. However, the penetration depth is not that high to cause the clot rupture and provide small pieces that can be dangerous.

2.10. Assessing MFMMAT under flow conditions

At the final stage of the experiments, we decided to consider the possibility of increasing the TR in the flow system. Particle behavior and vortex formation in the presence of flow can occur in a completely different way. At the same time, it is known that the presence of a flow critically affects the rate of clot dissolution.[68] We assembled a 1 mm diameter PDMS flow-through setup (Fig. 9A). The flow velocity (2 mL min^{-1}) was selected based on the wall shear rate in the veins, which is 15–200 s^{-1} and could increase to 10 000 s^{-1} after the onset of thrombosis.[69,70] Shear rate can be calculated as

$$\gamma = \frac{\Delta V}{h} \tag{3}$$

where ΔV is the difference between fluid speed on the border of the capillary and the clot, and h is the distance between the clot and the

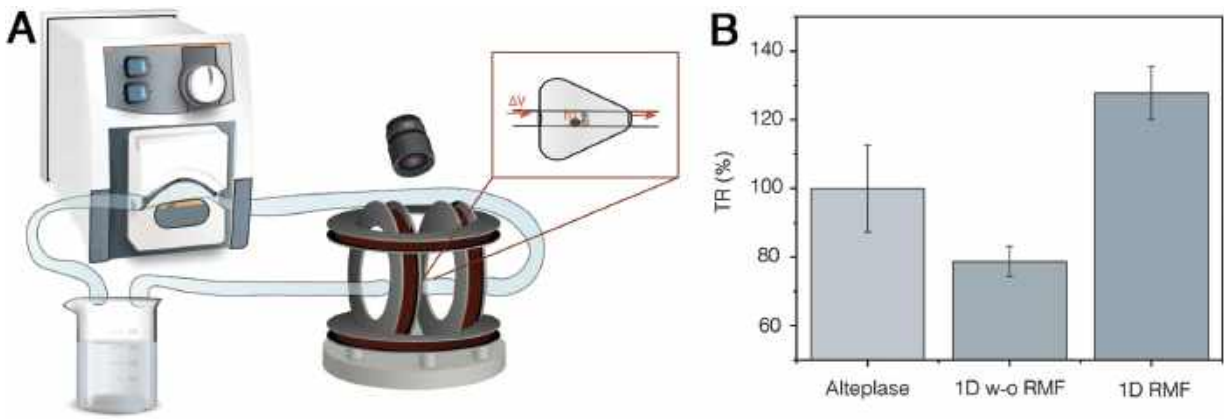

Fig. 9 (A) The scheme of flow setup. A peristaltic pump was connected *via* silicon tubes to a 1 mm PDMS channel. The clot was formed and placed in the channel lumen, so the distance h between the clot and channel wall was ~0.5 mm. A nylon filter was placed behind the clot to prevent its moving. (B) TR by thrombolytic alone, with, and w/o RFM. In the presence of RMF, TR increased by 27.8 ± 7.7%, while in the absence – decreased by 22.3 ± 4.4%.

capillary wall (Fig. 9A). In our case, the shear rate is approximately 340 s^{-1} considering the average clot size 0.5 × 0.5 mm. Additionally, we used another thrombolytic – alteplase which is a tissue plasminogen activator. The measured TR is presented in Fig. 9B.

In the absence of RMF, we observed a relatively similar (compared to static condition) reduction in TR by 22.3 ± 4.4%. However, in the presence of RMF, TR increased by 27.8 ± 7.7%. The increase was more than twice lower as in the static condition. Our observation showed no formation of vortices, so the mixing was executed by moving media itself. It is worth noting that the acoustic and rotating magnetic field application could stabilize the particle vortices in flow conditions and could be a subject of future investigation.[49] Nevertheless, the absence of vortices and increase in the TR allows us to suggest that it can be connected with the clot's mechanical disrupting. Such disrupting can be caused by particles and their aggregates stuck in the clot upon flowing near the clot border.

4. Conclusion

The development of new methods of thrombosis treatment is indisputably important in the face of ever-increasing deaths from this disease. In our work, we attempted to systematically study the effects of magnetic particles in the case of magnetic field-mediated mechanically-assisted thrombolysis. Following our first intention to show the differences between various shapes of magnetic nanoparticles, we proved that dimensional anisotropy plays an essential role in thrombolysis mediation. Particles in the forms of chains (1D) and spiky spheres (3D) increased scuPA effectiveness to *ca.* 175%. The primary mechanism underlying the enhancement of enzymatic activity lies in the superposition of two processes: the mechanical disturbance of fibrin mesh and intensified mass transfer in clot proximity. Both of these processes are closely related to the frequency of the external rotating magnetic field. Mixing particle behavior can be effectively executed in the frequency range of 25–100 Hz, while higher frequencies lead to the shift to rupture behavior. Even though our particles have noticeable saturation magnetization, the targeting issue is still a limiting factor for magnetic delivery. Particles and magnetic field should be precisely located in the clot vicinity to affect the clot lysis process. Ensuring these processes is much easier in the case of venous thrombosis. We pointedly showed that aged blood clots from vein blood could be effectively lysed with just moderate application of RMF. The experiments under flow conditions showed the potential of MFMMAT in conditions close to real cases. Additionally, the described results are independent of the type of enzymes and can be scaled to other thrombolytic drugs, which is definitely a subject of further research.

5. Materials and methods

5.1. Materials

Iron(II) chloride tetrahydrate ≥98.5%, iron(III) chloride hexahydrate ≥99%, sodium borohydride, pyrrole, citric acid, NaOH, iron(II) sulfate heptahydrate, MTT were purchased from Sigma-Aldrich (USA). DMEM culture medium, fetal bovine serum, gentamicin, PBS were purchased from Biolot (Russia). Aqueous ammonia solution (≥27.5%), hydrogen peroxide (30%), and DMSO were purchased from Vecton (Russia). Platelet-free lyophilized normal human plasma (PFP) and thrombin were purchased from Technologia Standart (Russia). scuPA lyophilized powder 2 000 000 IU was purchased from the National Medical Research Center for Cardiology (Moscow, Russia). Alteplase (Actilyse®) was purchased from Boehringer Ingelheim International GmbH (Germany). For all applications, deionized water (18 MΩ) was used (Millipore, USA).

5.2. Synthesis of spherical magnetite nanoparticles (designated as 0D particles)

A stable magnetite hydrosol was prepared by the ultrasonically assisted co-precipitation method described by Drozdov *et al.*[26] 2.5 g $FeCl_2{\cdot}4H_2O$ and 5 g $FeCl_3{\cdot}6H_2O$ (Fe^{2+}/Fe^{3+} molar ratio = 0.7) was dissolved in 100 mL of water under constant stirring (500 rpm). Then, 10 mL of aqueous ammonia (20%) was added to this solution under constant stirring (500 rpm) at room temperature for 5 min. The formed magnetite precipitate was collected using a magnet and washed with water until neutral pH. The washed black precipitate was mixed with 100 mL of water and subjected to ultrasonic treatment (37 kHz, 110 W) under constant stirring (300 rpm) for 120 min. The mass fraction of the resulting magnetite sol was 2.2 wt%.

5.3. Synthesis of chain-shaped magnetite particles (designated as 1D particles)

A chain-shaped particle of Fe_3O_4 was prepared by the chemical reduction method from $FeCl_3$ precursor, and $NaBH_4$ as the reducing agent in the presence of the pyrrole as a capping agent as described by Ankamwar *et al.*[27] 0.27 g $FeCl_3{\cdot}6H_2O$ and 0.570 mL C_4H_5N were dissolved in 20 mL of water. 0.75 g $NaBH_4$ was dissolved in 10 mL of water and added dropwise to the mixture mentioned above under vigorous magnetic stirring. The entire solution becomes dark and eventually turns completely black. The formed magnetite precipitate was collected with a magnet and washed with water until neutral pH.

5.4. Synthesis of plate-shaped magnetite particles (designated as 2D particles)

Magnetic plate-shaped particles were synthesized by the ligand-controlled co-precipitation method. 1 g NaOH and 0.1 g $C_6H_8O_7$ were dissolved in 50 mL of water. The solution was heated up to 90 °C in a 250 mL round-bottomed flask and degassed under argon. Simultaneously, $FeCl_3{\cdot}6H_2O$ (0.7 g) and $FeCl_2{\cdot}4H_2O$ (1 g) were dissolved in 5 mL of water. The solution of iron salts was added to NaOH/citric acid solution dropwise. The reaction was kept at 90 °C for 1 hour. The precipitate was washed with water and ethanol several times. The final product was collected in the form of black powder after drying under a vacuum at room temperature.

5.5. Synthesis of sea urchins-like magnetite particles (designated as 3D particles)

The synthesis of sea urchin-like particles is based on a modified hydrothermal synthesis of goethite nanorods[71] and recently

described.[72] 0.7 g of iron(II) sulfate heptahydrate was dissolved in 21 mL of water, and 6 mL of unstabilized hydrogen peroxide was added in one step under 500 rpm stirring. The resulting orange colloidal solution was placed in a 30 mL PTFE hydrothermal beaker, sealed, and transferred to a stainless steel autoclave. After that, the autoclave was placed in a muffle furnace, heated to 160 °C, kept at this temperature for 20 hours, and naturally cooled to room temperature. In the case of highly crystalline hematite particles, the temperature was increased up to 200 °C. The resulting colloidal solution was centrifuged, washed with water four times, and freeze-dried. For dry reduction, 100 mg of powder was heated up to 350 °C in a tube furnace in the flow of argon to remove moisture. The reduction was performed under the H_2 atmosphere for 2 hours. The sample was then cooled down to room temperature.

5.6. Preparation of model clots

Model clots were prepared by mixing equal volumes of platelet-free normal human plasma (prepared from lyophilized powder according to specification) with thrombin solution (4 IU mL^{-1}). The clots were left for 1 minute in ambient conditions and then used for experiments.

Blood clots were obtained from healthy male Wistar rats of the SPF category weighing 250 ± 10% g. Narcotization was performed with isoflurane in the SomnoSuite small animal anesthesia device (Kent Scientific, USA). Blood was taken by puncture of the posterior *vena cava*. Blood samples were placed in uncoated PP tubes and left in a freezer at +4 °C for three days. The clot was then removed from the tubes and dissected into more convenient pieces *ex tempore*.

5.7. Thrombolysis efficacy assessment

Lyophilized scuPA was dissolved in deionized water to a concentration of 0.8 mg mL^{-1} (89 350 IU mL^{-1}) and stored at +4 °C for no more than five days. For assessing the effect of particle shape and mixing on micro-level, particles (10 μL, 20 mg mL^{-1}) and scuPA (10 μL) were poured once onto the model clot separately. The experiments last for 12 minutes. For the experiment with the blood clot, scuPA was poured on the clot every 10 minutes, while the experiments last for 30 minutes. As a measure of efficiency, the clot surface area was analyzed using ImageJ free software (NIH, USA). After the measurement, the TR for all experiments was calculated as slope tangent and normalized on scuPA TR.

5.8. RMF setup

A rotating magnetic field (RFM) was created in the custom-build TOR 3D device (“Nanomaterials”, Russia), which has three pairs of axially-positioned Helmholtz coils. The magnetic field in the experimental chamber is uniform in each direction. The device allows an operator to use 2 out of 3 pairs of coils simultaneously. Frequency can be adjusted in the range of 1–200 Hz with a 0.1 Hz step. The maximum magnetic flux density in the center of the experiment chamber is 15 ± 2% mT. X and Y coils (*i.e.*, horizontal plane) and 10 mT magnetic flux density were used for all the experiments. Slow-motion videos were captured with Phantom Miro C110 high-speed camera at a capturing speed of 1000 fps.

5.9. Flow setup

The flow system was based on polydimethylsiloxane (PDMS) channels. The resin (Sylgard 184, Dow Corning Corp.) and Sylgard 184 curing agent (10 wt% of PDMS) were mixed and then degassed in a desiccator for 20 minutes. The channel shape was set using a copper wire of the required diameter (typically, 1 mm). The mold was poured with liquid PDMS and placed in an oven at 60–75 °C for 1 hour for curing. Then the wire was carefully removed from the mold. The obtained channels were completely optically transparent.

The resulting PDMS channel with desired shape and diameter was connected to a system of silicone tubes. The silicone tubes were connected to a peristaltic pump. A nylon filter and a fibrin clot were placed in the lumen of the PDMS channel. After that, a solution of 20% PFP with the studied particles and thrombolytic enzyme was pumped through tubes. The lysis process was recorded using an optical microscope. Area change was calculated using ImageJ (NIH, USA) image processing software.

5.10. Particles characterization

For SEM examination, a drop of particle solution was poured on the standard SEM sample table and dried under a vacuum. Samples were observed on Tescan VEGA 3 SBH at 10 kV. X-Ray diffraction spectra were obtained on Apex Duo (Bruker) at 1.5418 A (Cu Kα). Magnetic properties were measured on the VersaLab Quantum Design magnetometer. Hydrodynamic size and ζ-potential were measured on Photocor Compact Z (Russia) using standard parameters.

5.11. Cytotoxicity evaluation

Cytotoxicity of synthesized particles was assessed through standard MTT assay on HCT116 cells. Cells on the 4th passage were seeded on TC-treated 96-well culture plates and grew 24 hours for ~50% confluence. Particles were freeze-dried and redispersed in culture media (DMEM, 10% FBS, 50 μg mL^{-1} gentamicin) to a starting concentration of 400 μg mL^{-1}. Cells were incubated with particles for 24, 48, and 72 hours. 40 μL of MTT (2.5 mg mL^{-1}) were added to each well, containing 200 μL of media, for 1.5 hours, 37 °C. Further, the media was discarded, each well was washed once with PBS, and 200 μL of DMSO was added for 15 min at 37 °C. The plate was vigorously shaken for 30 s to provide uniform dissolution of formazan crystals, and the optical density of each well was measured on Tecan Infinite F50 at 570 nm. The optical density of control (untreated) cells was taken as 100% of metabolic activity.

5.12. Statistics

All of the experiments were repeated thrice unless otherwise stated. The data points presented in the figures are mean values with error bars showing standard deviation.

Conflicts of interest

The authors declare no conflicts of interest.

Acknowledgements

The work was supported by Ministry of Science and Higher Education of Russian Federation Grant no 075-15-2019-1896. The work of V. Vinogradov was supported by Ministry of Science and Higher Education of Russian Federation goszadanie no 2019-1075. The X-ray powder diffraction studies were performed on Rigaku SmartLab 3 diffractometer of the engineering center of the Saint-Petersburg State Technological Institute (Technical University).

References

1 M. Heron, *Natl. Vital Stat. Rep.*, 2019, **68**, 1–77.
2 H. K. Chew, T. Wun, D. J. Harvey, H. Zhou and R. H. White, *J. Clin. Oncol.*, 2007, **25**, 70–76.
3 B. Smith and G. Tefera, *J. Surg. Res.*, 2011, **166**, 45.
4 X. Li, L. Ling, C. Li and Q. Ma, *Med.*, 2017, 96.
5 Y. Li, J. Wang, Y. Gao, J. Zhu, M. G. Wientjes and J. L. S. Au, *AAPS J.*, 2011, **13**, 585–597.
6 C. S. Brazel and N. A. Peppas, *J. Controlled Release*, 1996, **39**, 57–64.
7 T. W. Chung, S. S. Wang and W. J. Tsai, *Biomaterials*, 2008, **29**, 228–237.
8 M. Juenet, R. Aid-Launais, B. Li, A. Berger, J. Aerts, V. Ollivier, A. Nicoletti, D. Letourneur and C. Chauvierre, *Biomaterials*, 2018, **156**, 204–216.
9 M. Zamanlu, M. Farhoudi, M. Eskandani, J. Mahmoudi, J. Barar, M. Rafi and Y. Omidi, *J. Drug Target.*, 2018, **26**, 95–109.
10 A. S. Pitek, Y. Wang, S. Gulati, H. Gao, P. L. Stewart, D. I. Simon and N. F. Steinmetz, *Mol. Pharm.*, 2017, **14**, 3815–3823.
11 R. Vankayala, S. R. Corber, J. T. Mac, M. P. Rao, M. Shafie and B. Anvari, *Macromol. Biosci.*, 2018, **18**(4), 1700379.
12 J. V. Nuzhina, A. A. Shtil, A. Y. Prilepskii and V. V. Vinogradov, *J. Drug Delivery Sci. Technol.*, 2019, **54**, 101282.
13 Y. H. Ma, S. Y. Wu, T. Wu, Y. J. Chang, M. Y. Hua and J. P. Chen, *Biomaterials*, 2009, **30**, 3343–3351.
14 J. P. Chen, P. C. Yang, Y. H. Ma and T. Wu, *Carbohydr. Polym.*, 2011, **84**, 364–372.
15 Y. H. Ma, Y. W. Hsu, Y. J. Chang, M. Y. Hua, J. P. Chen and T. Wu, *J. Magn. Magn. Mater.*, 2007, **311**, 342–346.
16 M. Wang, J. Zhang, Z. Yuan, W. Yang, Q. Wu and H. Gu, *J. Biomed. Nanotechnol.*, 2012, **8**, 624–632.
17 N. Serov, A. Prilepskii, A. Sokolov and V. Vinogradov, *ChemNanoMat*, 2019, **5**, 1267–1271.
18 R. Cheng, W. Huang, L. Huang, B. Yang, L. Mao, K. Jin, Q. Zhuge and Y. Zhao, *ACS Nano*, 2014, **8**, 7746–7754.
19 J. Hu, S. Huang, L. Zhu, W. Huang, Y. Zhao, K. Jin and Q. Zhuge, *ACS Appl. Mater. Interfaces*, 2018, **10**, 32988–32997.
20 T. O. Tasci, D. Disharoon, R. M. Schoeman, K. Rana, P. S. Herson, D. W. M. Marr and K. B. Neeves, *Small*, 2017, **13**(36), 1700954.
21 S. Laurent, D. Forge, M. Port, A. Roch, C. Robic, L. Vander Elst and R. N. Muller, *Chem. Rev.*, 2008, **108**, 2064–2110.
22 D. V. Kladko, A. S. Falchevskaya, N. S. Serov and A. Y. Prilepskii, *Int. J. Mol. Sci.*, 2021, **22**, 5266.
23 A. Y. Prilepskii, A. F. Fakhardo, A. S. Drozdov, V. V. Vinogradov, I. P. Dudanov, A. A. Shtil, P. P. Bel'Tyukov, A. M. Shibeko, E. M. Koltsova, D. Y. Nechipurenko and V. V. Vinogradov, *ACS Appl. Mater. Interfaces*, 2018, **10**, 36764–36775.
24 J. N. Tiwari, R. N. Tiwari and K. S. Kim, *Prog. Mater. Sci.*, 2012, **57**, 724–803.
25 R. G. D. Andrade, S. R. S. Veloso and E. M. S. Castanheira, *Int. J. Mol. Sci.*, 2020, 21.
26 A. S. Drozdov, V. Ivanovski, D. Avnir and V. V. Vinogradov, *J. Colloid Interface Sci.*, 2016, **468**, 307–312.
27 B. Ankamwar and A. Thorat, *J. Chem.*, 2012, **2013**, 537976.
28 N. R. Jana, L. Gearheart and C. J. Murphy, *Chem. Commun.*, 2001, 617–618.
29 K. C. Huang and S. H. Ehrman, *Langmuir*, 2007, **23**, 1419–1426.
30 K. Ranoszek-Soliwoda, E. Tomaszewska, E. Socha, P. Krzyczmonik, A. Ignaczak, P. Orlowski, M. Krzyzowska, G. Celichowski and J. Grobelny, *J. Nanopart. Res.*, 2017, **19**, 273.
31 S. Shinohara, N. Eom, E. J. Teh, K. Tamada, D. Parsons and V. S. J. Craig, *Langmuir*, 2018, **34**, 2595–2605.
32 W. Schärtl, *Adv. Mater.*, 2000, **12**, 1899–1908.
33 J. Liang, M. Luo, C. Yang, J. Fang and L. Li, *Cryst. Res. Technol.*, 2011, **46**, 493–496.
34 R. M. Cornell and U. Schwertmann, *The Iron Oxides*, 2003, 185–199.
35 R. N. Panda, N. S. Gajbhiye and G. Balaji, *J. Alloys Compd.*, 2001, **326**, 50–53.
36 M. H. Carvalho, R. J. S. Lima, C. T. Meneses, W. S. D. Folly, V. H. V. Sarmento, A. A. Coelho and J. G. S. Duque, *J. Appl. Phys.*, 2016, **119**, 093909.
37 K. Enpuku, A. L. Elrefai, T. Yoshida, T. Kahmann, J. Zhong, T. Viereck and F. Ludwig, *J. Appl. Phys.*, 2020, **127**, 133903.
38 I. Campos-Silva, M. Palomar-Pardavé, R. Pérez Pastén-Borja, O. Kahvecioglu Feridun, D. Bravo-Bárcenas, C. López-García and R. Reyes-Helguera, *Surf. Coat. Technol.*, 2018, **349**, 986–997.
39 A. Vaitkuviene, V. Kaseta, J. Voronovic, G. Ramanauskaite, G. Biziuleviciene, A. Ramanaviciene and A. Ramanavicius, *J. Hazard. Mater.*, 2013, **250–251**, 167–174.
40 V. V. Chrishtop, V. A. Mironov, A. Y. Prilepskii, V. G. Nikonorova and V. V. Vinogradov, *Nanotoxicology*, 2021, **15**, 167–204.
41 J. Yu, L. Yang and L. Zhang, *Int. J. Rob. Res.*, 2018, **37**, 912–930.
42 S. Hassanpour, H. J. Kim, A. Saadati, P. Tebon, C. Xue, F. W. van den Dolder, J. Thakor, B. Baradaran, J. Mosafer, A. Baghbanzadeh, N. R. de Barros, M. Hashemzaei, K. J. Lee, J. Lee, S. Zhang, W. Sun, H. J. Cho, S. Ahadian, N. Ashammakhi, M. R. Dokmeci, A. Mokhtarzadeh and A. Khademhosseini, *Small*, 2020, 16.
43 D. E. Vaughan, *J. Thromb. Haemostasis*, 2005, **3**, 1879–1883.
44 G. Tsivgoulis, A. H. Katsanos, P. D. Schellinger, M. Köhrmann, P. Varelas, G. Magoufis, M. Paciaroni, V. Caso, A. W. Alexandrov, E. Gurol and A. V. Alexandrov, *Stroke*, 2018, **49**, 232–235.

45 M. Dentz, T. Le Borgne, A. Englert and B. Bijeljic, *J. Contam. Hydrol.*, 2011, **120–121**, 1–17.
46 S. H. Lee, D. Van Noort, J. Y. Lee, B. T. Zhang and T. H. Park, *Lab Chip*, 2009, **9**, 479–482.
47 D. J. Klingenberg, J. C. Ulicny and M. A. Golden, *J. Rheol.*, 2007, **51**, 883–893.
48 S. G. Sherman, A. C. Becnel and N. M. Wereley, *J. Magn. Magn. Mater.*, 2015, **380**, 98–104.
49 D. Ahmed, D. Hauri, A. Sukhov, D. Rodrigue, M. Gian, J. Harting and B. Nelson, *Nat. Mach. Intell.*, 2021, **3**, 116–124.
50 F. Ji, D. Jin, B. Wang and L. Zhang, *ACS Nano*, 2020, **14**, 6990–6998.
51 F. Martínez-Pedrero, *Adv. Colloid Interface Sci.*, 2020, **284**, 102233.
52 J. Faraudo, J. S. Andreu, C. Calero and J. Camacho, *Adv. Funct. Mater.*, 2016, **26**(22), 3837–3858.
53 D. A. Gabriel, K. Muga and E. M. Boothroyd, *J. Biol. Chem.*, 1992, **267**(34), 24259–24263.
54 A. S. Wolberg, *Blood Rev.*, 2007, **21**(3), 131–142.
55 R. L. Medcalf, C. E. Hagemeyer and K. Alt, *J. Thromb. Haemost.*, 2018, **16**, 615–617.
56 D. H. Kim, E. A. Rozhkova, I. V. Ulasov, S. D. Bader, T. Rajh, M. S. Lesniak and V. Novosad, *Nat. Mater.*, 2010, **9**, 165–171.
57 T. M. Ma, J. S. VanEpps and M. J. Solomon, *Biophys. J.*, 2017, **113**(9), 2100–2109.
58 K. M. Weigandt, N. White, D. Chung, E. Ellingson, Y. Wang, X. Fu and D. C. Pozzo, *Biophys. J.*, 2012, **103**(11), 2399–2407.
59 I. K. Piechocka, R. G. Bacabac, M. Potters, F. C. Mackintosh and G. H. Koenderink, *Biophys. J.*, 2010, **98**(10), 2281–2289.
60 I. M. Le-Deygen, K. Y. Vlasova, E. O. Kutsenok, A. D. Usvaliev, M. V. Efremova, A. O. Zhigachev, P. G. Rudakovskaya, D. Y. Golovin, S. L. Gribanovsky, E. V. Kudryashova, A. G. Majouga, Y. I. Golovin, A. V. Kabanov and N. L. Klyachko, *Nanomedicine*, 2019, **21**, 102065.
61 M. G. Beckman, W. C. Hooper, S. E. Critchley and T. L. Ortel, *Am. J. Prev. Med.*, 2010, 38.
62 M. Koupenova, B. E. Kehrel, H. A. Corkrey and J. E. Freedman, *Eur. Heart J.*, 2017, **38**, 785–791.
63 S. Z. Goldhaber, M. F. Meyerovitz, E. Braunwald, D. Green, R. L. Vogelzang, P. Citrin, J. Heit, M. Sobel, H. Brownell Wheeler, D. Plante, H. Kim, A. Hopkins, M. Tufte and D. Stump, *Am. J. Med.*, 1990, **88**, 235–240.
64 R. K. Popuri and S. Vedantham, *Arterioscler., Thromb., Vasc. Biol.*, 2011, **31**, 479–484.
65 P. Prandoni, M. Frulla, D. Sartor, A. Concolato and A. Girolami, *J. Thromb. Haemost.*, 2005, **3**, 401–402.
66 J. W. Weisel and R. I. Litvinov, *Blood*, 2013, **121**, 1712–1719.
67 G. Schwieder, W. Grimm, H. J. Siemens, B. Flor, A. Hilden, E. Gmelin, H. J. Friedrich and T. Wagner, *J. Thromb. Haemost.*, 1995, **74**, 1240–1243.
68 M. Anand, K. Rajagopal and K. R. Rajagopal, *J. Theor. Med.*, 2003, **5**(3–4), 183–218.
69 S. Gogia and S. Neelamegham, *Biorheology*, 2015, **52**(5–6), 319–335.
70 A. Rana, E. Westein, B. Niego and C. E. Hagemeyer, *Front. Cardiovasc. Med.*, 2019, **6**, 141.
71 Y. Dong, H. Yang, R. Rao and A. Zhang, *J. Nanosci. Nanotechnol.*, 2009, **9**, 4774–4779.
72 D. V. Kladko, M. A. Zakharzhevskii and V. V. Vinogradov, *J. Phys. Chem. Lett.*, 2020, **11**(21), 8989–8996.